Epitaxial Growth of Large-Area Monolayers and van der Waals Heterostructures of Transition-Metal Chalcogenides via Assisted Nucleation

Akhil Rajan,* Sebastian Buchberger, Brendan Edwards, Andela Zivanovic, Naina Kushwaha, Chiara Bigi, Yoshiko Nanao, Bruno K. Saika, Olivia R. Armitage, Peter Wahl, Pierre Couture, and Phil D. C. King*

The transition-metal chalcogenides include some of the most important and ubiquitous families of 2D materials. They host an exceptional variety of electronic and collective states, which can in principle be readily tuned by combining different compounds in van der Waals heterostructures. Achieving this, however, presents a significant materials challenge. The highest quality heterostructures are usually fabricated by stacking layers exfoliated from bulk crystals, which – while producing excellent prototype devices – is time consuming, cannot be easily scaled, and can lead to significant complications for materials stability and contamination. Growth via the ultra-high vacuum deposition technique of molecular-beam epitaxy (MBE) should be a premier route for 2D heterostructure fabrication, but efforts to achieve this are complicated by non-uniform layer coverage, unfavorable growth morphologies, and the presence of significant rotational disorder of the grown epilayer. This work demonstrates a dramatic enhancement in the quality of MBE grown 2D materials by exploiting simultaneous deposition of a sacrificial species from an electron-beam evaporator during the growth. This approach dramatically enhances the nucleation of the desired epi-layer, in turn enabling the synthesis of large-area, uniform monolayers with enhanced quasiparticle lifetimes, and facilitating the growth of epitaxial van der Waals hetero-structures.

1. Introduction

The layered transition-metal chalcogenides (TMCs) are formed of blocks of covalently bonded transition-metals (M) and chalcogens (X = S, Se, Te), which are stacked together with only weak van der Waals (vdW) forces between the layers. The most famous structure is of MX_2 type, but the family contains a plethora of other binary (e.g., M_2X_3) and ternary (e.g., $M_2Y_2X_6$, Y = Si, Ge) phases. Their van der Waals nature allows for the ready isolation of single layers of these compounds, which together host a huge variety of electronic, magnetic, and collective states: from spin-valley locked semiconductors[1–3] to electrically tunable magnets[4,5] and superconducting and charge-density wave (CDW) systems.[6–9] Most commonly, the fabrication of TMC monolayers (MLs) is performed by mechanical exfoliation, in the same way as for the isolation of graphene from bulk graphite.[10] This has been shown to yield monolayer flakes of high

A. Rajan, S. Buchberger, B. Edwards, A. Zivanovic, N. Kushwaha, C. Bigi, Y. Nanao, B. K. Saika, O. R. Armitage, P. Wahl, P. D. C. King
SUPA, School of Physics and Astronomy
University of St Andrews
St Andrews KY16 9SS, UK
E-mail: ar289@st-andrews.ac.uk; pdk6@st-andrews.ac.uk
S. Buchberger, A. Zivanovic
Max Planck Institute for Chemical Physics of Solids
Nöthnitzer Strasse 40, 01187 Dresden, Germany

N. Kushwaha
STFC Central Laser Facility
Research Complex at Harwell
Harwell Campus, Didcot OX11 0QX, UK

P. Wahl
Physikalisches Institut
Universität Bonn
Nussallee 12, 53115 Bonn, Germany

P. Couture
Ion Beam Centre
University of Surrey
Guildford, Surrey GU2 7XH, UK

**ADVANCED
SCIENCE NEWS**

www.advancedsciencenews.com
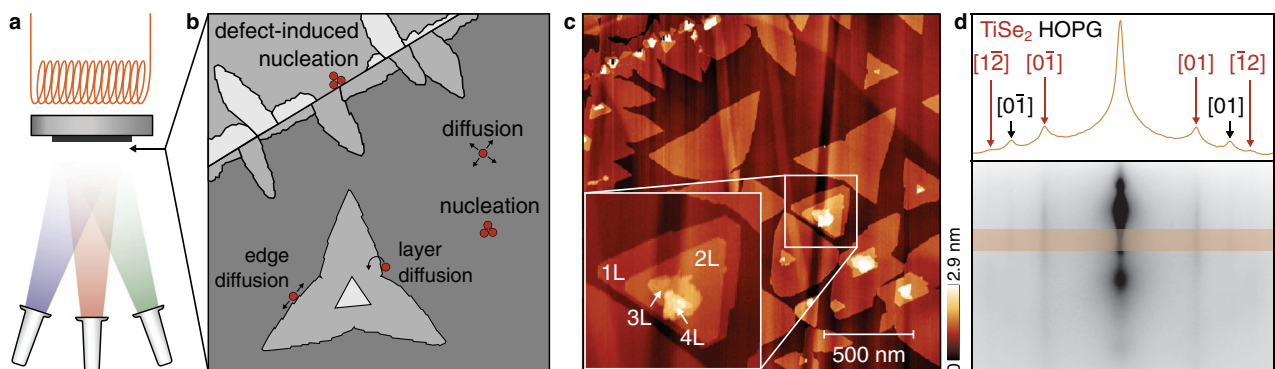
**ADVANCED
MATERIALS**

www.advmat.de

Figure 1. MBE growth of 2D transition-metal chalcogenides. a) Schematic of an MBE growth setup showing high-purity molecular beams focused towards a heated substrate in the centre of a UHV chamber. b) Schematic illustration of the various options available to physisorbed species at the substrate surface during growth. c) AFM image showing the surface morphology of a typical TiSe$_2$ monolayer growth on an HOPG substrate. d) RHEED image during the growth of the sample shown in (c). The line cut shows clear diffraction streaks from both HOPG (black) and TiSe$_2$ (red).

crystallinity and low defect density,[11,12] which can be stacked together to form state-of-the-art prototypical devices through a careful and time-consuming transfer process.[13–16] While recently, methods have been developed to perform such device assembly in an ultra-high vacuum (UHV) environment,[17,18] devices are typically fabricated in air or an inert gas-filled glove box, which can lead to complications via the incorporation of contaminants into the assembled device structure[19,20] and the degradation of air-sensitive materials.[21]

As an alternative to this challenging top-down assembly of 2D TMCs, chemical vapor deposition (CVD) has become established as the de facto standard for the bottom-up synthesis of 2D materials.[22,23] This technique has been demonstrated to be effective in producing large-area monolayers and bilayers with good control of material thickness up to the wafer scale.[24–26] However, the higher synthesis temperatures required by CVD (typically in the range of 850–1100 °C) raises some challenges, especially in the case of synthesising heterostructures using a two-step route, where a lower temperature is required for the second or subsequent layers in order to protect the bottom layer.[27,28] Lowering the synthesis temperature can cause the formation of randomly-aligned domains,[25,26] which can occur in particular if the thermodynamically stable state cannot be reached in the early nucleation period. Additionally, impurities from the precursor molecules used in the growth can become incorporated into the grown layer.[29,30]

In principle, molecular-beam epitaxy (MBE) should be the ideal method to overcome these challenges. It is a precise UHV-based deposition technique, with growth proceeding on a single-crystalline substrate from molecular beams of ultra-pure elemental sources (**Figure 1a**). It is well-established as the "gold standard" for the epitaxial growth of conventional semiconductors and their heterostructures, yielding devices with the highest electron mobilities,[31] lowest defect densities and most uniform layer structures.[32,33] However, efforts to utilize MBE for the fabrication of monolayers or heterostructures of 2D materials have, to date, proved extremely challenging.

To illustrate the complexities observed, we show in Figure 1 the results of a typical MBE growth of a representative 2D-TMC (here TiSe$_2$ grown atop a graphite (HOPG) substrate, see

Experimental Section). A large number of small inhomogeneous islands originate from nucleation of the epilayer growth at substrate step edges, which leads to the formation of unfavorable growth fronts resulting in rotated domains and multilayer growth patches (Figure 1b,c). A lower density of larger islands are formed away from these step edges. These evolve from much-preferred spontaneous or substrate defect-mediated nucleation clusters. The absence of surface dangling bonds in vdW materials means that, under ideal conditions, diffusing adatoms on the growth surface would be captured at the active growth edge of such clusters, undergoing edge diffusion (see Figure 1b) and causing the growth to progress dominantly in-plane, resulting in a layer-by-layer growth mode. In reality,[34] however, the first TMC monolayer island acts as an energetically favorable substrate for adatoms with lower mobility. The result is a partial coverage of the substrate, with exposed substrate regions co-existing with multi-layer epi-islands as evident in our atomic force microscopy (AFM) measurements shown in Figure 1c, as well as via the presence of pronounced diffraction streaks from the epilayer and the underlying graphite substrate in reflection high-energy electron diffraction (RHEED) measurements (Figure 1d).

Further increase in the monolayer coverage will also increase the multilayer coverage: to date, even the most successful attempts to use MBE for the growth of large-area TMCs have generally not yielded individual islands with sizes greater than ca. one micrometer.[34,35] While a proof of principle for larger-area growth has been demonstrated via a complex multi-step growth procedure,[36] this required extremely high growth temperatures – likely leading to significant chalcogen vacancy formation in the film – and impractically slow growth rates. A widely applicable growth method for the large-area growth of uniform epitaxial monolayers of TMCs has thus remained elusive. Here, we report how such improved growth modes can readily be achieved via the co-evaporation of a sacrificial species from an electron beam (e-beam) evaporator during the epitaxial growth. We show how this can lead to continuous epitaxial monolayers that have excellent azimuthal order, improved electronic lifetimes, and whose size is limited only by the growth substrate. Our work thus demonstrates the first growth of large-area vdW heterostructures via an all-UHV approach.
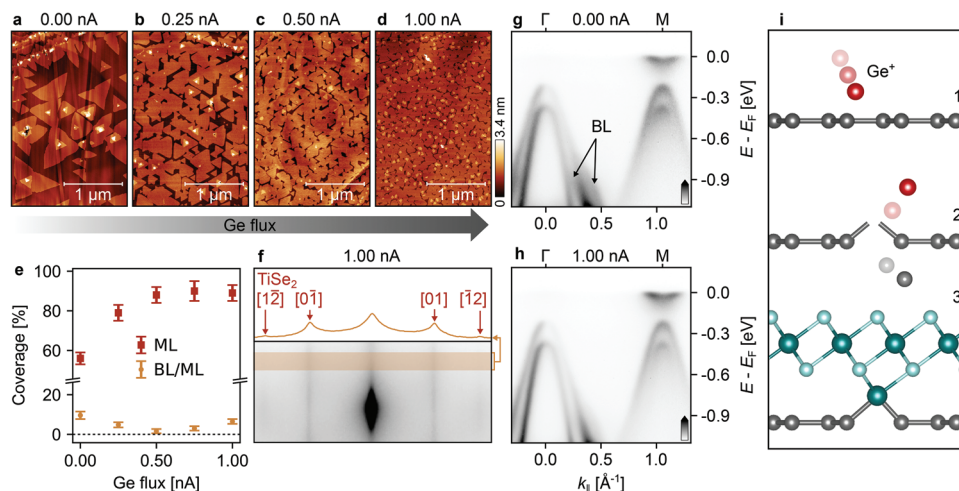
**ADVANCED
SCIENCE NEWS**

www.advancedsciencenews.com

**ADVANCED
MATERIALS**

www.advmat.de

Figure 2. Influence of Ge co-evaporation on the growth of TiSe$_2$. a–d) AFM topographies of TiSe$_2$ samples grown on an HOPG substrate with co-evaporation of small quantities of Ge. An increasing flux of Ge from 0 nA to 1 nA shows the striking influence of the additive on the epilayer morphology (see Figure S12 (Supporting Information) for corresponding height profiles from the AFM). e) Dependence of monolayer (ML) surface coverage, and bi- and multi-layer formation relative to the monolayer area (BL/ML) on the additive flux, as estimated from our AFM measurements. f) RHEED image for the film grown with 1 nA Ge flux showing only the TiSe$_2$ film streaks present. Analysis of the corresponding line cut indicates a spacing consistent with pure ML TiSe$_2$. g) ARPES spectrum of a TiSe$_2$ sample grown without Ge and measured at $T = 17$ K, showing the electronic structure of ML TiSe$_2$ in the CDW phase. Signatures of initial bilayer (BL) formation are also evident. (h) Same as (g) on a sample grown with 1 nA of Ge, showing the unperturbed electronic structure of ML TiSe$_2$ and persistence of its CDW. i) Schematic illustration of the Ge e-beam assisted MBE growth process for 2D TMC materials. An incoming excited Ge ion (step 1) induces a defect in the van der Waals substrate (step 2), leading to dangling bonds which promote nucleation of the TMC island (step 3).

2. Results and Discussion

2.1. E-Beam Assisted Epitaxial Growth of Monolayer TiSe$_2$

Key to growing larger-area monolayers of TMCs is the suppression of multilayer formation and enhancing the seeding of the growth by increasing the adatom cluster-based nucleation sites. We show in **Figure 2** how this can be achieved by employing deposition of a non-reactive sacrificial species from an e-beam evaporator during the MBE growth. We show this here for Ge as the sacrificial species, enhancing the growth of a TiSe$_2$ layer on an HOPG substrate. In the traditional growth mode, with evaporation of only Ti and Se (Figure 2a), the growth progresses in the regular manner discussed above, with a large number of small fractal islands forming due to nucleation at defects and a smaller number of larger fractal-triangular islands forming from intrinsic nucleation clusters, which themselves show substantial multilayer formation. Indeed, the monolayer coverage for the sample shown here is less than 60%, while already there is around 10% of the film surface covered by two or more layers (Figure 2e).

Adding the deposition of a trace amount of Ge from an e-beam evaporator during the growth, with all other growth parameters remaining unchanged, we find a dramatic and immediate improvement in the obtained film morphology and monolayer coverage. We measure the supply of Ge as a charged particle current through the integrated flux-meter of the used electron-beam evaporator. Adding just 0.25 nA of Ge during the growth (Figure 2b), we find an increase in the monolayer coverage to around 80% – indicating a significant increase in growth rate – while the bilayer coverage drops to less than 5%. Moreover, the fractal-triangular morphology [34] (Figure 1b) has transformed into a more thermodynamically favorable case of fully triangular

islands. The growth rate and monolayer coverage are further increased by increasing the Ge flux up to 1 nA, without significant increase in the bilayer coverage (Figure 2a–e), leading to the formation of a near-continuous monolayer (Figure 2d). Indeed, the corresponding RHEED measurements now show only the diffraction streaks from the epilayer (Figure 2f), without signatures of the substrate (cf. Figure 1d), confirming a near-complete monolayer coverage across the sample.

While the morphological properties of the epilayer are clearly enhanced by the co-evaporation of Ge during the growth, a key question is whether this detrimentally affects the monolayer properties in another way. We confirmed from the RHEED streak spacing (Figure 2f) that the TiSe$_2$ lattice constant is identical to that of layers grown without the additional Ge co-evaporation (Figure 1d), and equal within error to that of bulk TiSe$_2$. As a sensitive test of the influence of the Ge supplied on the electronic properties of the monolayer, we show in Figure 2g,h the electronic structure of samples grown with and without Ge supply as measured by in situ angle-resolved photoemission (ARPES, see Experimental Section). While the broad band structure is qualitatively similar between the two samples, we find that the measured linewidth is in fact around 30% smaller for the sample grown with Ge, pointing to an enhanced carrier lifetime and reduced quasiparticle scattering (see Figure S1, Supporting Information). In both samples, a clear replica of the dispersive valence band states from the Γ-point are observed at the M-point, indicating that a charge-density wave instability that this system hosts is unaffected by the use of Ge. Furthermore, the conduction band filling is identical within our resolution for the two samples, meaning that the Ge does not cause any additional Se vacancies to form, or lead to other carrier doping in the sample. Meanwhile, signatures of an additional band splitting (labeled BL in

ADVANCED
SCIENCE NEWS

www.advancedsciencenews.com

**ADVANCED
MATERIALS**

www.advmat.de

Figure 2g), which arises due to bilayer interactions are strongly suppressed for the sample grown with Ge as compared to the one without Ge, in line with our AFM measurements showing the dramatic enhancement of the ratio of monolayer:bilayer coverage in the two samples (Figure 2e).

Together, our combined AFM and ARPES measurements thus suggest that both the mesoscale structure and microscopic sample quality are enhanced for our Ge e-beam assisted growth method presented here. Moreover, they suggest that there is negligible incorporation of Ge as impurities in films grown in this way, something we have also confirmed via chemical analysis (Figures S2 and S3, Supporting Information), while atomic-scale imaging via STM shows excellent crystalline order and low defect densities of ca. 0.1% (Figure S4, Supporting Information). We thus conclude that there is no significant incorporation of the Ge into the growing film.

A key question, therefore, is what causes the dramatic enhancement to the epitaxial growth demonstrated here. In analogy to the use of surface-active species as surfactants in the MBE growth of conventional semiconductors,[37–42] one possibility is that the mobile Ge adatoms can be more readily caught into an active edge of a growing epi-island than for the Ti atoms, occupying the metal vacancy sites until they are preferentially replaced by Ti adatoms as the growth proceeds.[43,44] Interestingly, however, we do not find the same enhancement in growth quality when Ge is evaporated from an effusion cell, even when the Ge flux is tuned over several orders of magnitude (Figure S5, Supporting Information). This rules out any significant direct surfactant effect of the Ge atoms.

Instead, it points to a crucial role of the specific mode of delivery of the sacrificial species. In this respect, we note that Ge evaporated from an effusion cell consists of mainly low-energy neutral molecules, while, in comparison, e-beam evaporators in general introduce a significant quantity of highly excited ions. In fact, ion-beam assisted deposition - where the substrate is continuously bombarded with a high energy ion-beam - is known to be a powerful method for tuning growth morphologies of elemental metals,[45–47] thought mainly to occur via the transfer of kinetic energy to the adatoms and thus enabling increased surface diffusion and adhesion.

While the Ge ions could play such a role here, the incoming ion beam may also induce substrate defects, which in turn would act as new nucleation sites, seeding the growth (Figure 2i).[48] To distinguish between these scenarios, we have separated the exposure of the substrate to the Ge e-beam from the growth of the TiSe₂ layer. As shown in Figure S6 (Supporting Information), we find that this two-step growth process yields almost identical monolayer TiSe₂ films to growths performed with co-evaporation of the Ge with the Ti. This strongly points to enhanced nucleation as the primary driver of the improved growth methodologies we find here.

We have further confirmed this by studying both the initial stages of the growth (Figure S7, Supporting Information) and how this evolves with deposition time to yield smooth monolayer growth (Figure S8, Supporting Information). Specifically, we find that a dramatically-enhanced nucleation site density leads to the initial growth of a larger number of small growth domains. With the increased number of islands, and thus smaller inter-island separation, the diffusing adatoms that land on the substrate surface can more easily reach a growing island, explaining the enhanced growth rate that we observe. Moreover, with the now smaller island size, adatoms that land on the island surface can readily migrate to the edge of the island where they can participate in edge diffusion, contributing to the growth of the initial monolayer rather than seeding bi/multi-layer growth as was evident in Figure 1c. Only after the longest deposition times, as the initial monolayer is essentially completed, do small additional triangular islands start to form on the growth surface, reflecting the start of nucleation for the second layer. It will be interesting to explore the detailed energetics of this process further in future theoretical calculations. Already here, however, our experimental measurements demonstrate how a true layer-by-layer growth mode can be realized for the first time in van der Waals epitaxy.

2.2. Generality of the Nucleation-Assisted Growth Process in 2D TMCs

We show in **Figure 3** that this approach is not limited to TiSe₂ growth, but can be effectively applied across a wide range of chalcogenide-based 2D materials growth. We first consider the sister transition-metal dichalcogenide VSe₂, which can be expected to behave similarly to TiSe₂, except that a lower metal atom mobility leads to a more fractal-like branched morphology at the growth temperature of 600 °C used here (see Table S1, Supporting Information for detailed growth conditions) when not utilizing the Ge e-beam, with nucleation occurring predominantly at substrate step edges (Figure 3a). When Ge is co-evaporated from the e-beam evaporator, however (Figure 3b), the free nucleation of the islands is substantially increased - similar to, but even more significantly than, the case of TiSe₂. Indeed, we find that the islands have merged into a near-complete monolayer of VSe₂, with only few gaps or bilayer islands visible. Electronic structure measurements of the VSe₂ films grown with and without Ge show similar band dispersions, with characteristic signatures of the charge-density wave ground state[9] visible in both cases. As already observed in monolayer TiSe₂, we find a reduced linewidth in the spectrum of monolayer VSe₂ grown with our e-beam method, indicating reduced scattering and confirming the improved crystalline quality.

Our method, however, is not limited to transition-metal dichalcogenides, and we show in Figure 3c–f how this can be used to enable the epitaxial growth of single Cr₂X₃ (X = Se, Te) quintuple-layer structures, a compound of current interest as a putative 2D magnet.[49,50] Although Cr₂Se₃ is a nominally stable compound, our attempts to obtain high-quality monolayers of these samples using conventional methods repeatedly suffered from poor intrinsic quality as judged by broad signals in our spectroscopic measurements (Figure 3c). In contrast, with enhanced nucleation from our e-beam-assisted approach, we find monolayer (with 1 ML indicating one Se-Cr-Se-Cr-Se block) thickness uniformity. The quality of our spectroscopic data is, in turn, markedly enhanced, with much sharper linewidths and better resolved bands. As well as being of strong practical benefit to facilitate future electronic structure studies of this system, this further points to a striking ability of our e-beam-assisted approach to not only enhance the large-scale structures, but also the microscopic crystalline structure and reduce defect densities.
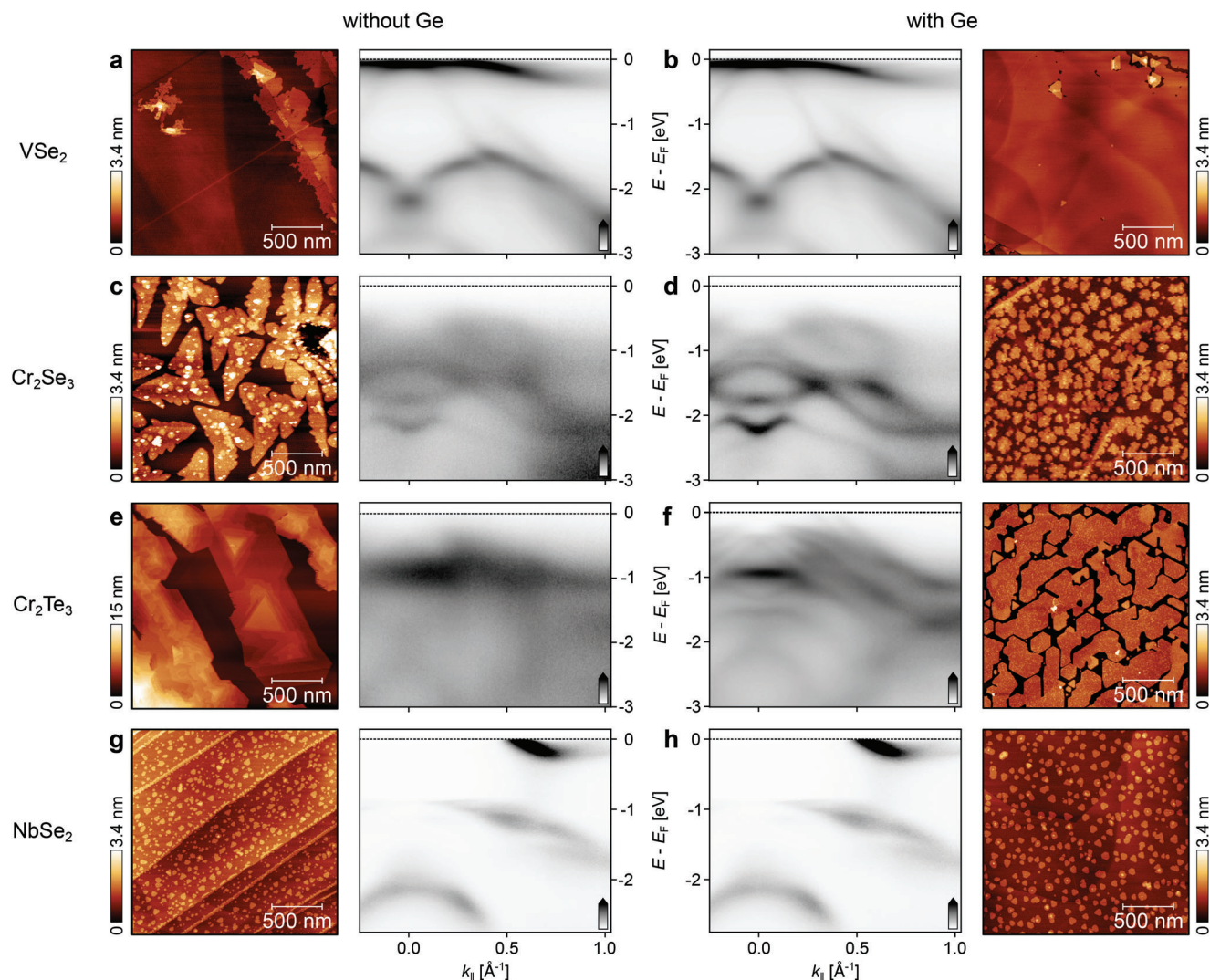
**ADVANCED
SCIENCE NEWS**

www.advancedsciencenews.com

**ADVANCED
MATERIALS**

www.advmat.de

Figure 3. Influence of co-evaporation of Ge from an e-beam evaporator on the growth of various TMCs. 2×2 µm AFM images and ARPES spectra measured along normal emission at 10 K from four different materials: a,b) VSe_2, c,d) $Cr_{2-\delta}Se_3$, e,f) $Cr_{2-\delta}Te_3$ and g,h) $NbSe_2$, for samples grown without (a,c,e,g) and with (b,d,f,h) Ge co-evaporation (1 nA). While substantial multilayer formation is found without Ge suppply, the growths grown with Ge co-evaporation exhibit almost exclusively monolayer terraces (see also Figure S12, Supporting Information). Due to randomly-oriented azimuthal domains in the substrate, smaller than the probing beam spot, the ARPES measurements are azimuthally averaged, but still show a clear improvement in quasiparticle lifetimes with the addition of Ge during the growth. Note that for the quintuple-layer Cr-based materials, a range of different Cr concentrations are possible as these form a family of self-intercalation compounds. We thus refer to these as $Cr_{2-\delta}X_3$ here.

We find similar, although arguably even more dramatic, changes for the Cr_2Te_3 sister compound. With the larger Te orbitals and stronger inter-layer bonding, we find that 3D island growth is favored without the Ge co-evaporation (see the highly multi-layer growth in Figure 3e, and the diffuse and poorly-resolved spectra in our ARPES measurements). However, with our e-beam-assisted growth method (Figure 3f), a transition to a 2D layer-by-layer growth mode is obtained, with near-complete monolayer coverage and negligible bilayer growth, while the ARPES measurements show a similar improvement in measured linewidth as for the Cr_2Se_3 compound.

The influence of the e-beam assisted growth is more subtle in the case of heavier transition-metals such as Nb (Figure 3g,h). Here, the transition metal of interest is already evaporated from

an e-beam evaporator which, combined with the low mobility of the Nb and high sticking co-efficient on the surface, means that a significant number of nucleation sites are already expected without the aid of the Ge ions from the e-beam (Figure 3g). The island sizes and shapes (Figure 3h) are thus only slightly enhanced when using the new technique. Nonetheless, we do note a large suppression in the formation of chain-like features on the surface when utilizing the Ge. These are metal-metal chains that can form due to the low surface diffusion lengths of the metal adatoms here, which in turn can act as unfavorable, long nucleation step edges. Thus, while the effect of the Ge e-beam is not as dramatic for $NbSe_2$ as for the other systems investigated here, we conclude that it does still make a positive contribution in efforts to stabilize more uniform monolayers. Consistent with the
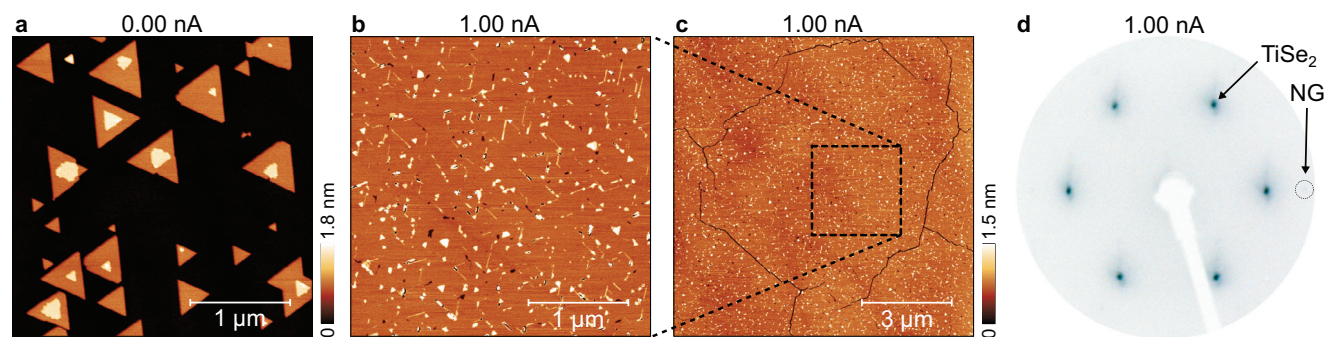
Figure 4. Large-area growth of ML TiSe$_2$ on natural graphite. a) AFM topography of a TiSe$_2$ sample grown on a natural graphite substrate (NG) with no Ge flux, showing low coverage and significant bilayer formation. b) Sample grown with 1 nA of Ge flux showing near-complete ML coverage with only small gaps in the film and negligible multi-layer formation. c) Larger area topography of the sample shown in (b). d) LEED image from the Ge e-beam-assisted sample growth, showing negligible rotational disorder and good epitaxial alignment of the film (TiSe$_2$) and NG substrate.

more subtle change in the growth morphology, we find our measured ARPES spectra to be much more similar between the two samples than for the systems discussed above.

We note that the e-beam aided growth method proposed here is not limited to Ge as a sacrificial species. Other species can be used, as long as they are evaporable from the e-beam source and do not form stable bonds with the chalcogen species under the growth conditions used. As an example, we show in Figure S9 (Supporting Information) the case of using Ag as an active species, evaporated from the e-beam source, where we find a similar increase in surface coverage and nucleation as for the use of Ge. In both cases, co-evaporation of just the sacrificial species with the chalcogen using typical flux and temperature parameters yield no coverage on the growth substrate following 2 h of growth (Figure S10, Supporting Information). This confirms that these do not form stable binary compounds under the growth conditions used, and are thus able to induce nucleation sites but without incorporating into the grown film.

This points to the generality of the e-beam assisted growth process here, and the wide flexibility in materials choice that can be made to facilitate the growth of TMC films in the desired layer-by-layer manner. Another advantage of our method is that it allows the use of growth conditions (such as very low metal fluxes and high temperatures) that would otherwise yield impractically low growth rates, but which become feasible with dramatic enhancements in growth rates found here (e.g. Figure S9, Supporting Information). It should also be readily possible to extend the approach demonstrated here to the growth of important S-based TMC compounds, where we would expect similar considerations to apply.

2.3. Growth of Large-Area Monolayers and van der Waals Heterostructures

Despite the generality of the approach, it is still crucial to utilize the highest quality growth substrate in order to avoid unfavorable nucleation sites from the substrate itself. While the HOPG substrates used in the studies discussed above are ideal for easy preparation and growth investigations, even the highest quality commercially-available HOPG is comprised of small in-plane grains that are rotationally misaligned, which prevents the growth of continuous large-area films across the grain boundary.

We show instead growth of TiSe$_2$ on a natural graphite substrate in **Figure** 4a. Here, the surface is atomically flat and well-ordered over a length scale of tens of micrometers. The higher quality of the growth substrate is already visible in our measurements without utilising the e-beam assisted growth (Figure 4a), by the lack of nucleation at step edges. While this leads to the growth of sharp and well-ordered triangular domains, the surface coverage is very low, and most of the TiSe$_2$ islands already exhibit the onset of significant bilayer formation.

In contrast, by using the Ge co-evaporation, we obtain a near-complete monolayer coverage, with almost no exposed substrate visible (<2 %) and almost no bilayer regions present (<3 %, Figure 4b). In fact, we find the grown layer to be essentially completely uniform across the substrate, as shown in our 10 × 10 μm AFM topography in Figure 4c, with small cracks now appearing which may have resulted from the relaxation of residual strains during the cooling process following the growth. Similar AFM measurements are found at macroscopically different regions on the substrate, suggesting uniform coverage. Moreover, our low-energy electron diffraction (LEED) measurements shown in Figure 4d indicate that the epilayer grows with excellent azimuthal order across the entire substrate (our LEED beam spot probes a region of ca. 0.5 mm diameter). The substrate Bragg spots are only very weakly visible – again reflecting the full coverage – but are in excellent alignment with the TiSe$_2$ spots, again reflecting negligible rotational disorder and an excellent epitaxial registry between the substrate and the monolayer grown atop, despite the large lattice mismatch. We note that the formation of some domain boundaries are still visible in the AFM measurements in Figure 4b, where initial growth domains merge. This likely reflects the formation of mirror twin domain boundaries. These could themselves be further suppressed by use of a threefold symmetric substrate such as hBN or MoS$_2$, where careful control of the growth conditions can be used to favor the formation of a single mirror domain from the initial stages of the growth.[51]

Already, the enhanced size and uniformity of the as-grown monolayers obtained here opens the door, for the first time, for using MBE to grow epitaxial vdW heterostructures layer by layer. As a proof-of-principle of this approach, we show in **Figure** 5a TiSe$_2$/VSe$_2$ heterostructure grown atop a natural graphite
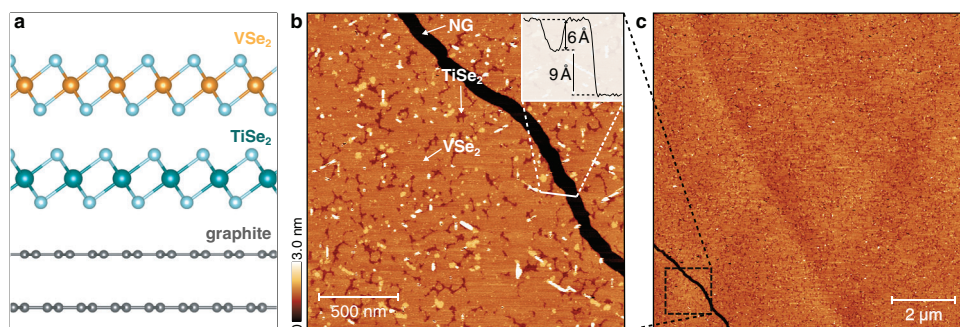
Figure 5. Epitaxial growth of large-area vdW heterostructures. a) Crystal structure of the heterostructure (side view) showing the graphite substrate and monolayer VSe$_2$ on top of monolayer TiSe$_2$. b,c) AFM topographies showing the morphology of the natural graphite/TiSe$_2$/VSe$_2$ heterostructure, again showing a near-complete and uniform coverage of each layer in the heterostructure stack.

substrate (Figure 5a). The initial TiSe$_2$ monolayer was grown as described above, while the growth temperature was reduced to 400°C for deposition of the top VSe$_2$ layer to reduce any potential intermixing at the TiSe$_2$ - VSe$_2$ interface. As shown in Figure 5b,c, the VSe$_2$ layer has almost fully covered the TiSe$_2$ layer beneath, although we stopped the growth just before a full VSe$_2$ monolayer is completed. This leaves small gaps in the VSe$_2$ layer through which we can use AFM to confirm the TiSe$_2$/VSe$_2$ layer stacking sequence (see inset in Figure 5b and Figure S11, Supporting Information).

3. Conclusion

Our work thus demonstrates how enhanced nucleation induced by self-ions of sacrificial species can be used to dramatically enhance the MBE growth of monolayer transition-metal dichalcogenides and vdW materials. Combined with judicious choice of the growth substrate, we have shown how this can be used to realize uniform monolayers across multi-micron length scales, which opens new possibilities to, e.g., perform transport measurements on such MBE-grown monolayers or to lithographically define device structures. To further facilitate all-epitaxial device strucutres, it will be interesting to extend our growth studies to other, non van der Waals, substrates such as silicon. Already for the van der Waals substrates investigated here, we have shown how the improved materials quality is reflected not only in the mesoscopic morphological properties, but also in the carrier lifetimes as judged from electronic structure measurements, and have demonstrated how our growth method facilitates the epitaxial growth of vertical heterostructures of distinct 2D materials. This is particularly exciting for air-sensitive materials, including most of the materials studied here, as it provides a route to fabricate such large-area and high-quality heterostructure samples in a fully UHV environment, opening new possibilities for realizing proximity coupling at their interfaces to control the plethora of emergent states that 2D TMCs host.

4. Experimental Section

MBE Growth: The 2D TMCs were grown using a DCA R450 MBE system, on highly oriented pyrolytic graphite (HOPG) and natural graphite (NG) substrates. The growth chamber had a base pressure of $\approx 2 \times 10^{-10}$

mbar and a working pressure of $\approx 2 \times 10^{-9}$ mbar during growth. Substrates were degassed at $\approx 200°C$ in the load lock for ca. 12 h before transferring to the growth chamber. The quality of the substrate surface was monitored using in situ RHEED. Prior to growth, the substrates were further annealed at 700 – 800 °C for ≈ 30 min before cooling to growth temperature. Full growth parameters for all samples were listed in the Supporting Information. Growth temperatures were measured by a thermocouple placed behind the substrate heater, which likely overestimates the true surface temperature by around 150–200°C.

For transition metal sources, high temperature effusion cells were utilized containing 3N5 pure Ti, 3N5 pure Cr, and 4N pure V, and an e-beam evaporator containing 3N5 pure Nb. The Ge and Ag sacrificial species were also evaporated from the same Focus EFM 3T triple e-beam evaporator. A valved cracker cell was used to generate a 5N pure Se flux. The cracker zone of the Se source was maintained at an elevated temperature of 500°C during growth, to generate cracked Se monomers or dimers and to prevent condensation near the valve. 5N pure Te was evaporated from a home-built Knudsen cell. A beam-equivalent pressure (BEP) of 1×10^{-7} mbar and 5×10^{-8} mbar for the Se and Te sources was used, respectively, as estimated by positioning a retractable beam flux monitoring ion gauge in front of the substrate, just before the growth. While the low flux of the transition-metal sources make it hard to obtain an accurate estimate of their BEP using this method, it was estimated that they were approximately two orders of magnitude lower than for the chalcogen sources, to combat the higher vapor pressures and lower sticking coefficients of the chalcogen species.

Film Characterization: ARPES and XPS were performed on samples transferred under vacuum, utilizing a Specs Phoibos 225 analyzer, and probed using 21.2 eV and 1486.7 eV photons from a He plasma lamp and a monochromated X-ray source, respectively. The samples were cooled to 10 K (17 K) for the ARPES measurements in Figure 3 (Figure 2), while the XPS measurements were also performed at 10 K. LEED measurements were performed using an OCI LEED optics, using an electron energy of 100 eV, with the samples again transferred from the growth chamber under UHV. STM measurements were performed in a home-built UHV STM operating at temperatures down to 1.5K. Bias voltages were applied to the sample, with the tip at virtual ground. The sample was transferred from the growth system to the STM using a vacuum suitcase.

The morphologies of the as-grown samples were analyzed ex situ, after removing the samples from vacuum and immediately transferring them to an Ar-filled glovebox. A Park Systems NX10 AFM placed in the glovebox was used for all topographic measurements shown here, with measurements performed in non-contact mode. The quantitative analysis of surface areas was done by grain selection based on height thresholds. The compositional stoichiometry of epilayers was further probed using Rutherford Backscattering Spectrometry (RBS) with a 2 MeV He$^+$ beam, with a spot size of 10 μm × 10 μm and a beam current of 1 nA. RBS spectra were analyzed with SIMNRA.[52] Particle-induced X-ray emission

(PIXE) data were collected using 2.5 MeV He$^+$ beam to better characterize Ge, with a spot size of 5 μm × 5 μm. Samples for RBS and PIXIE were capped with thin amorphous layers of Se before removing them from the growth chamber.

Supporting Information

Supporting Information is available from the Wiley Online Library or from the author.

Conflict of Interest

The authors declare no conflict of interest.

Data Availability Statement

The data that support the findings of this study are openly available in the University of St Andrews Research Portal at https://doi.org/10.17630/9d07b1cb-b75c-4a0e-87ca-d7ba7649857c, reference number [53].

Keywords

2D materials, electronic properties, molecular beam epitaxy, nucleation

[1] D. Xiao, G.-B. Liu, W. Feng, X. Xu, W. Yao, *Phys. Rev. Lett.* **2012**, *108*, 196802.

[2] K. F. Mak, K. He, J. Shan, T. F. Heinz, *Nat. Nanotechnol.* **2012**, *7*, 494.

[3] H. Zeng, J. Dai, W. Yao, D. Xiao, X. Cui, *Nat. Nanotechnol.* **2012**, *7*, 490.

[4] Z. Wang, T. Zhang, M. Ding, B. Dong, Y. Li, M. Chen, X. Li, J. Huang, H. Wang, X. Zhao, Y. Li, D. Li, C. Jia, L. Sun, H. Guo, Y. Ye, D. Sun, Y. Chen, T. Yang, J. Zhang, S. Ono, Z. Han, Z. Zhang, *Nat. Nanotechnol.* **2018**, *13*, 554.

[5] I. A. Verzhbitskiy, H. Kurebayashi, H. Cheng, J. Zhou, S. Khan, Y. P. Feng, G. Eda, *Nat. Electron.* **2020**, *3*, 460.

[6] M. M. Ugeda, A. J. Bradley, Y. Zhang, S. Onishi, Y. Chen, W. Ruan, C. Ojeda-Aristizabal, H. Ryu, M. T. Edmonds, H.-Z. Tsai, A. Riss, S.-K. Mo, D. Lee, A. Zettl, Z. Hussain, Z.-X. Shen, M. F. Crommie, *Nat. Phys.* **2016**, *12*, 92.

[7] P. Chen, Y.-H. Chan, X.-Y. Fang, Y. Zhang, M. Y. Chou, S.-K. Mo, Z. Hussain, A.-V. Fedorov, T.-C. Chiang, *Nat. Commun.* **2015**, *6*, 8943.

[8] L. J. Li, E. C. T. O'Farrell, K. P. Loh, G. Eda, B. Özyilmaz, A. H. Castro Neto, *Nature* **2016**, *529*, 185.

[9] J. Feng, D. Biswas, A. Rajan, M. D. Watson, F. Mazzola, O. J. Clark, K. Underwood, I. Marković, M. McLaren, A. Hunter, D. M. Burn, L. B. Duffy, S. Barua, G. Balakrishnan, F. Bertran, P. Le Fèvre, T. K. Kim, G. van der Laan, T. Hesjedal, P. Wahl, P. D. C. King, *Nano Lett.* **2018**, *18*, 4493.

[10] K. S. Novoselov, D. Jiang, F. Schedin, T. J. Booth, V. V. Khotkevich, S. V. Morozov, A. K. Geim, *Proc. Natl. Acad. Sci.* **2005**, *102*, 10451.

[11] M. Chhowalla, H. S. Shin, G. Eda, L.-J. Li, K. P. Loh, H. Zhang, *Nat. Chem.* **2013**, *5*, 263.

[12] B. W. H. Baugher, H. O. H. Churchill, Y. Yang, P. Jarillo-Herrero, *Nano Lett.* **2013**, *13*, 4212.

[13] J. Song, F.-Y. Kam, R.-Q. Png, W.-L. Seah, J.-M. Zhuo, G.-K. Lim, P. K. H. Ho, L.-L. Chua, *Nat. Nanotechnol.* **2013**, *8*, 356.

[14] B. Hunt, J. D. Sanchez-Yamagishi, A. F. Young, M. Yankowitz, B. J. LeRoy, K. Watanabe, T. Taniguchi, P. Moon, M. Koshino, P. Jarillo-Herrero, R. C. Ashoori, *Science* **2013**, *340*, 1427.

[15] Y. Cao, V. Fatemi, S. Fang, K. Watanabe, T. Taniguchi, E. Kaxiras, P. Jarillo-Herrero, *Nature* **2018**, *556*, 43.

[16] C. Jin, E. C. Regan, A. Yan, M. Iqbal Bakti Utama, D. Wang, S. Zhao, Y. Qin, S. Yang, Z. Zheng, S. Shi, K. Watanabe, T. Taniguchi, S. Tongay, A. Zettl, F. Wang, *Nature* **2019**, *567*, 76.

[17] W. Wang, N. Clark, M. Hamer, A. Carl, E. Tovari, S. Sullivan-Allsop, E. Tillotson, Y. Gao, H. de Latour, F. Selles, J. Howarth, E. G. Castanon, M. Zhou, H. Bai, X. Li, A. Weston, K. Watanabe, T. Taniguchi, C. Mattevi, T. H. Bointon, P. V. Wiper, A. J. Strudwick, L. A. Ponomarenko, A. V. Kretinin, S. J. Haigh, A. Summerfield, R. Gorbachev, *Nat. Electron.* **2023**, *6*, 981.

[18] A. Grubišić-Čabo, M. Michiardi, C. E. Sanders, M. Bianchi, D. Curcio, D. Phuyal, M. H. Berntsen, Q. Guo, M. Dendzik, *Adv. Sci.* **2023**, *10*, 2301243.

[19] S. J. Haigh, A. Gholinia, R. Jalil, S. Romani, L. Britnell, D. C. Elias, K. S. Novoselov, L. A. Ponomarenko, A. K. Geim, R. Gorbachev, *Nat. Mater.* **2012**, *11*, 764.

[20] A. V. Kretinin, Y. Cao, J. S. Tu, G. L. Yu, R. Jalil, K. S. Novoselov, S. J. Haigh, A. Gholinia, A. Mishchenko, M. Lozada, T. Georgiou, C. R. Woods, F. Withers, P. Blake, G. Eda, A. Wirsig, C. Hucho, K. Watanabe, T. Taniguchi, A. K. Geim, R. V. Gorbachev, *Nano Lett.* **2014**, *14*, 3270.

[21] F. Ye, J. Lee, J. Hu, Z. Mao, J. Wei, P. X.-L. Feng, *Small* **2016**, *12*, 5802.

[22] H. Schmidt, S. Wang, L. Chu, M. Toh, R. Kumar, W. Zhao, A. H. Castro Neto, J. Martin, S. Adam, B. Özyilmaz, G. Eda, *Nano Lett.* **2014**, *14*, 1909.

[23] C. H. Naylor, W. M. Parkin, Z. Gao, H. Kang, M. Noyan, R. B. Wexler, L. Z. Tan, Y. Kim, C. E. Kehayias, F. Streller, Y. R. Zhou, R. Carpick, Z. Luo, Y. W. Park, A. M. Rappe, M. Drndić, J. M. Kikkawa, A. T. C. Johnson, *2D Mater.* **2017**, *4*, 021008.

[24] A. T. Hoang, K. Qu, X. Chen, J.-H. Ahn, *Nanoscale* **2021**, *13*, 615.

[25] T. Li, W. Guo, L. Ma, W. Li, Z. Yu, Z. Han, S. Gao, L. Liu, D. Fan, Z. Wang, Y. Yang, W. Lin, Z. Luo, X. Chen, N. Dai, X. Tu, D. Pan, Y. Yao, P. Wang, Y. Nie, J. Wang, Y. Shi, X. Wang, *Nat. Nanotechnol.* **2021**, *16*, 1201.

[26] L. Liu, T. Li, L. Ma, W. Li, S. Gao, W. Sun, R. Dong, X. Zou, D. Fan, L. Shao, C. Gu, N. Dai, Z. Yu, X. Chen, X. Tu, Y. Nie, P. Wang, J. Wang, Y. Shi, X. Wang, *Nature* **2022**, *605*, 69.

[27] X. Gong, X. Zhao, M. E. Pam, H. Yao, Z. Li, D. Geng, S. J. Pennycook, Y. Shi, H. Y. Yang, *Nanoscale* **2019**, *11*, 4183.

[28] T. Kang, T. W. Tang, B. Pan, H. Liu, K. Zhang, Z. Luo, *ACS Materials Au* **2022**, *2*, 665.

[29] X. Zhang, Z. Y. Al Balushi, F. Zhang, T. H. Choudhury, S. M. Eichfeld, N. Alem, T. N. Jackson, J. A. Robinson, J. M. Redwing, *J. Electron. Mater.* **2016**, *45*, 6273.

**ADVANCED
SCIENCE NEWS**

www.advancedsciencenews.com

**ADVANCED
MATERIALS**

www.advmat.de

[30] T. H. Choudhury, H. Simchi, R. Boichot, M. Chubarov, S. E. Mohney, J. M. Redwing, *Cryst. Growth Des.* **2018**, *18*, 4357.

[31] V. Umansky, M. Heiblum, Y. Levinson, J. Smet, J. Nübler, M. Dolev, *J. Cryst. Growth* **2009**, *311*, 1658.

[32] L. Li, J. Zhu, L. Chen, A. Davies, E. Linfield, *Opt. Express* **2015**, *23*, 2720.

[33] M. J. Manfra, *Annu. Rev. Condens. Matter Phys.* **2014**, *5*, 347.

[34] A. Rajan, K. Underwood, F. Mazzola, P. D. C. King, *Phys. Rev. Mater.* **2020**, *4*, 014003.

[35] W. Pacuski, M. Grzeszczyk, K. Nogajewski, A. Bogucki, K. Oreszczuk, J. Kucharek, K. E. Połczyńska, B. Seredyński, A. Rodek, R. Bożek, T. Taniguchi, K. Watanabe, S. Kret, J. Sadowski, T. Kazimierczuk, M. Potemski, P. Kossacki, *Nano Lett.* **2020**, *20*, 3058.

[36] D. Fu, X. Zhao, Y.-Y. Zhang, L. Li, H. Xu, A.-R. Jang, S. I. Yoon, P. Song, S. M. Poh, T. Ren, Z. Ding, W. Fu, T. J. Shin, H. S. Shin, S. T. Pantelides, W. Zhou, K. P. Loh, *J. Am. Chem. Soc.* **2017**, *139*, 9392.

[37] M. Copel, M. C. Reuter, E. Kaxiras, R. M. Tromp, *Phys. Rev. Lett.* **1989**, *63*, 632.

[38] J. Massies, N. Grandjean, *Phys. Rev. B* **1993**, *48*, 8502.

[39] L. X. Zheng, M. H. Xie, S. M. Seutter, S. H. Cheung, S. Y. Tong, *Phys. Rev. Lett.* **2000**, *85*, 2352.

[40] J. K. Shurtleff, S. W. Jun, G. B. Stringfellow, *Appl. Phys. Lett.* **2001**, *78*, 3038.

[41] R. D. Feldman, R. F. Austin, D. W. Kisker, K. S. Jeffers, P. M. Bridenbaugh, *Appl. Phys. Lett.* **1986**, *48*, 248.

[42] C. Y. Fong, M. D. Watson, L. H. Yang, S. Ciraci, *Model. Simul. Mater. Sci. Eng.* **2002**, *10*, R61.

[43] C. Bradford, C. O'Donnell, B. Urbaszek, A. Balocchi, C. Morhain, K. Prior, B. Cavenett, *Appl. Phys. Lett.* **2000**, *76*, 3929.

[44] L. Quagliano, B. Jusserand, F. Mollot, D. Orani, *Phys. E: Low-Dimens. Syst. Nanostructures.* **1998**, *2*, 824.

[45] P. J. Martin, H. A. Macleod, R. P. Netterfield, C. G. Pacey, W. G. Sainty, *Appl. Opt.* **1983**, *22*, 178.

[46] F. Smidt, *Int. Mater. Rev.* **1990**, *35*, 61.

[47] S. Esch, M. Breeman, M. Morgenstern, T. Michely, G. Comsa, *Surface science* **1996**, *365*, 187.

[48] M. Heilmann, V. Deinhart, A. Tahraoui, K. Höflich, J. M. J. Lopes, *npj 2D Mater. Appl.* **2021**, *5*, 70.

[49] Y. Wen, Z. Liu, Y. Zhang, C. Xia, B. Zhai, X. Zhang, G. Zhai, C. Shen, P. He, R. Cheng, L. Yin, Y. Yao, M. Getaye Sendeku, Z. Wang, X. Ye, C. Liu, C. Jiang, C. Shan, Y. Long, J. He, *Nano Lett.* **2020**, *20*, 3130.

[50] I. H. Lee, B. K. Choi, H. J. Kim, M. J. Kim, H. Y. Jeong, J. H. Lee, S.-Y. Park, Y. Jo, C. Lee, J. W. Choi, S. W. Cho, S. Lee, Y. Kim, B. H. Kim, K. J. Lee, J. E. Heo, S. H. Chang, F. Li, B. L. Chittari, J. Jung, Y. J. Chang, *ACS Appl. Nano Mater.* **2021**, *4*, 4810.

[51] H. Bana, E. Travaglia, L. Bignardi, P. Lacovig, C. E. Sanders, M. Dendzik, M. Michiardi, M. Bianchi, D. Lizzit, F. Presel, D. D. Angelis, N. Apostol, P. K. Das, J. Fujii, I. Vobornik, R. Larciprete, A. Baraldi, P. Hofmann, S. Lizzit, *2D Mater.* **2018**, *5*, 035012.

[52] M. Mayer, *AIP Conf. Proc.* **1999**, *475*, 541.

[53] A. Rajan, S. Buchberger, B. M. Edwards, A. Zivanovic, N. Kumari, C. Bigi, Y. Nanao, B. Saika, O. R. Armitage, P. Wahl, P. Couture, P. King, Epitaxial Growth of Large-area Monolayers and van der Waals Heterostructures of Transition-metal Chalcogenides via Assisted Nucleation, Dataset, University of St Andrews Research Portal, **2024**, https://doi.org/10.17630/9d07b1cb-b75c-4a0e-87ca-d7ba7649857c.

2402254 (9 of 9)